European Journal of Pharmaceutics and Biopharmaceutics 74 (2010) 377–387

Contents lists available at ScienceDirect

European Journal of Pharmaceutics and Biopharmaceutics

journal homepage: www.elsevier.com/locate/ejpb

Research paper

Investigation into the intragranular structures of microcrystalline cellulose and pre-gelatinised starch

Peter Laity [a,*], Andrew Cassidy [b], Jeremy Skepper [c], Bill Jones [b], Ruth Cameron [a]

[a] Department of Materials Science and Metallurgy, University of Cambridge, Cambridge, UK
[b] Department of Chemistry, University of Cambridge, Cambridge, UK
[c] Department of Physiology, University of Cambridge, Cambridge, UK

ARTICLE INFO

Article history:
Received 4 September 2009
Accepted in revised form 29 October 2009
Available online 1 November 2009

Keywords:
Small-angle X-ray scattering (SAXS)
Wide-angle X-ray scattering (WAXS)
Scanning electron microscopy (SEM)
Transmission electron microscopy (TEM)
Atomic force microscopy (AFM)
Nitrogen adsorption
Microcrystalline cellulose (MCC)
Starch 1500, pre-gelatinised starch (PGS)
Granule structure

SUMMARY

The internal structures of commercial spheronised microcrystalline cellulose (s-MCC) and pre-gelatinised starch (PGS) granules were investigated, using a range of methods. Results from scanning electron microscopy (SEM), transmission electron microscopy (TEM) and atomic force microscopy (AFM) revealed hierarchical structures, with dimensions ranging from nanometres to a few micrometres, for both materials. Residual fragments of plant cell walls, consisting largely of crystalline fibrillar bundles, were indicated within s-MCC granules, while PGS granules appeared to consist of densely packed spherical features. The lack of any obvious regular periodicity associated with the intragranular sub-structures was entirely consistent with the power-law behaviour of the small-angle X-ray scattering (SAXS) patterns from these materials. The presence of intragranular porosity was inferred from TEM, AFM and N_2-adsorption measurements, while the ability to deform these structures was clearly indicated by the irregular force–displacement curves recorded by AFM on the granule surfaces. Hence, the intragranular sub-structures observed for s-MCC and PGS appeared to be consistent with the possibility of entire granules undergoing affine deformation during compaction. Since this mechanism was postulated to explain changes in SAXS patterns from these materials following compaction, as reported elsewhere, the work reported here provides a considerably stronger basis for using 2D-SAXS to investigate powder compaction behaviour.

1. Introduction

Powder compaction is important in many diverse applications: the manufacture of ceramic, polymeric or metallic components by sintering; soil mechanics in agriculture or civil engineering and the production of pharmaceutical tablets. Consequently, it has been the subject of extensive research and a vast number of publications, describing both experimental investigations and numerical simulations; indeed, the importance of pharmaceutical applications alone [1–3] has stimulated a large part of this work. While this has provided a relatively clear picture of powder compaction on the macroscopic scale, however, much of the sub-microscopic detail is still missing. For example, finite element modelling (FEM), which treats a granular bed as a compressible continuum [4], is able to describe macroscopic behaviour with remarkable accuracy but ignores behaviour at or below the granular scale. At the other extreme, discrete models address the micro-mechanics of individual inter-granular contacts [5,6], but often depend on various simplifying assumptions, such as a relatively small number of monodispersed, spherical granules. The validity of the model used to represent granule deformation, which often assumes Hertzian contact mechanics [7], may also be open to question. Consequently, more detailed investigations into the internal sub-structures of granules and their response during compaction could provide very useful advances in the field.

Nevertheless, while granule shape and behaviour during powder compaction are widely recognised as important, the internal sub-structures of granules have received relatively little attention. The scarcity of published work investigating the links between intragranular sub-structure and compaction behaviour seems rather surprising, given the availability of well-established methods such as scanning electron microscopy (SEM), transmission electron microscopy (TEM) and several variants of atomic force microscopy (AFM). Amongst recent works, X-ray microtomography (XμT) was used by Rahmanian et al. [8] to investigate granules composed of calcium carbonate with a poly(ethylene glycol) binder, Boden et al. [9] to investigate polyethylene granules and Farber et al. [10] to study porous mannitol and lactose-MCC

* Corresponding author. Pfizer Institute for Pharmaceutical Materials Science, Department of Materials Science and Metallurgy, University of Cambridge, New Museums Site, Pembroke St., Cambridge CB2 3QZ, UK. Tel.: +44 1223 767059; fax: +44 1223 334567.
E-mail address: prl28@cam.ac.uk (P. Laity).

0939-6411/$ - see front matter © 2009 Elsevier B.V. All rights reserved.
doi:10.1016/j.ejpb.2009.10.006

granules. Suteu et al. [11] used SEM and nitrogen adsorption to investigate the pore structure and dye absorption capabilities of polyamide powders. However, these workers have not reported on the compaction behaviour of the materials used. From extensive investigations into the compaction of microcrystalline cellulose (MCC) granules, Johansson and co-workers [12–15] and Westermarck et al. [16] suggested that the dominant mechanisms during compaction were granule deformation and densification through the reduction of intragranular pore volume.

It was reported recently [17,18] that uniaxial compaction produced some interesting and significant changes in the small-angle X-ray scattering (SAXS) patterns from spheronised microcrystalline cellulose (s-MCC) and pre-gelatinised starch (PGS) granules, which are commonly used as pharmaceutical excipients. SAXS patterns measured using a two-dimensional 'area detector' (2D-SAXS) from these materials became elongated in the compaction direction, to an extent that increased with the compaction pressure applied or the relative density of the resulting tablet. Examination of scattering data obtained at different points across diametral sections provided a new method for quantifying the local density variations within the tablets, which were caused by friction between the powder and the compaction die – also known as the Janssen effect [19,20]. In addition, changes in orientation of the 'long axis' of the 2D-SAXS patterns revealed local variations in the effective compaction direction, with significant outward components evident close to the tablet sides.

SAXS measurements are well-established and widely used for investigating morphology [21,22]. It is known that scattering in the small-angle range (typically, the scattering angle, 2θ, from 0.1° to 3°) is associated with electron density variations over length-scales of roughly 1–100 nm. Hence, this can reveal information concerning the size, distribution and orientation of many different morphological features, including crystallinity or microphase separation in polymers, voids in porous materials, size and aggregation in colloidal dispersions and composition changes associated with surfaces or interfaces. In view of the versatility of SAXS measurements, including the possibility of spatially resolved studies using micro-beams or kinetic studies with millisecond temporal resolution, given a sufficiently bright X-ray source, it is somewhat surprising that no prior application to investigating powder compaction had been reported.

Although the initial studies [17,18] were largely empirical, they did demonstrate the possibility of using 2D-SAXS to investigate the effects of compaction conditions on density variations within tablets. Moreover, it is expected that a suitable analysis of the 2D-SAXS data should provide more quantitative information concerning the deformation behaviour of powder granules during compaction. Subsequent work [23] showed that the observed changes in 2D-SAXS patterns following compaction were consistent with affine deformation of the nanometre-scale morphology within granules. It was suggested that each powder granule was essentially composed of smaller structural sub-units and behaved similar to the macroscopic powder bed in response to compaction – albeit, on a smaller length-scale. This hypothetical behaviour appeared to be quite similar to that deduced by Johansson and co-workers [12–15] and Westermarck et al. [16] for compacted MCC powder.

The purpose of the present work is to investigate the morphologies within s-MCC and PGS granules and identify the likely origins of the X-ray scattering, in order to test the granule compaction hypothesis in more detail. Analyses were performed using combinations of SAXS, SEM, TEM, AFM and nitrogen adsorption measurements, to reveal the hierarchy of intragranular sub-structural features, over length-scales from micrometres down to nanometres. The results are discussed with respect to the expected compaction behaviour of these materials on the sub-granular scale and the associated changes in 2D-SAXS patterns.

2. Experimental

Two commercially available pharmaceutical tabletting materials were used: s-MCC (Celphere SCP100, Asahi-Kasei, Japan) and PGS (Starch 1500, Colorcon Ltd. Kent, UK).

2.1. Scanning electron microscopy

Superficial features of the s-MCC and PGS granules were investigated by SEM. A piece of conductive (carbon-impregnated) double-sided adhesive tape was affixed to an aluminium stub and a small amount of powder was sprinkled onto it. Excess powder was removed by gently blowing, before gold-coating, using an Emitech K550 sputter-coater (Quorum Technologies Ltd. Hailsham, UK), at 20 mA for 3 min. The samples were viewed using a JSM820 (JEOL Ltd. Tokyo, Japan) at 10 kV and 15 mm sample distance.

2.2. Fracturing or sectioning powder to reveal internal structure

Attempts at cryo-fracturing of powder granules 'as received' was unsuccessful. A sample of the powder was cryo-protected by dehydration to 100% ethanol, before freezing in propane cooled in liquid nitrogen. Subsequently fracturing with a cooled blade produced only fragments with completely amorphous surfaces.

Instead, powder was dehydrated in 100 % ethanol and embedded, using Quetol 651 epoxy resin (ethylene glycol diglycidal ether, 9 g), with non-enyl succinic anhydride (11.6 g), nadic methyl anhydride (5 g) as hardeners and benzyl dimethyamine (0.5 g) as accelerator (all supplied by Agar scientific, Stanstead, UK). This mixture was immediately cured by heating at 60 °C for 24 h. The resin castings, encapsulated but not infiltrated with resin, were trimmed to plane flat surfaces through the powder granules, using a glass knife. These sections were fixed onto SEM stubs using silver DAG (Agar scientific, Stanstead, UK), coated with 10 nm of gold using a Quorum Emitech K5775X sputter-coater (Quorum Emitech, Ashford, Kent, UK) and viewed by SEM with a field-emission gun (FEI XL30 FEGSEM, FEI, Eindhoven, The Netherlands).

2.3. Transmission electron microscopy

Powder was dehydrated in 100% ethanol and infiltrated in two changes of 100% dry acetonitrile. It was then stood for 24 h in a 1:1 volumetric mixture of acetonitrile and Quetol epoxy resin. The mixture was then changed to a 3:1 volumetric mixture of Quetol and acetonitrile for a further 24 h, followed by five daily changes in 100% Quetol resin, together with hardeners and accelerator. This was cured by heating at 60 °C for 24 h. Thin sections were cut using a diamond knife on a Leica Ultracut UCT (Leica, Vienna, Austria) and mounted on 300 mesh copper grids. After staining with uranyl acetate and lead citrate, the sections were viewed by TEM (FEI CM100) operated at 80 kV with a 10 μm objective aperture; images were recorded using a Deben AMT 16,000 digital camera (Deben, Woolpit, Suffolk, UK).

2.4. Atomic force microscopy

AFM images and force–displacement curves were recorded using a Multimode AFM (operated by a Nanoscope IIIa controller, interfaced with a Quadrex extender module, Veeco Instruments, Santa Barbara). Granules of s-MCC and PGS were dispersed on cleaved Muscovite mica, with electrostatic interactions holding the granules in place. Samples were imaged in air with an E scanner (13 μm × 13 μm maximum scan size) under normal conditions of room temperature (*ca.* 22 °C), atmospheric pressure and approximately 40% relative humidity. All images were recorded in tapping

mode using commercially available sharpened Si probes (FESP 18 series, Mikromasch, Estonia). The AFM probes were pressed against the mica to calibrate the photodiode response and the optical laser alignment was constant throughout the remainder of each experiment. Spring constants were determined via the Sader method [24]; this gave an average value of 2.61 N m^{-1} for the cantilevers used on s-MCC, while stiffer cantilevers (spring constant up to 40 N m^{-1}) were required to indent PGS granules. A sealed chamber was placed around the AFM and purged with dry N_2 for at least 1 h prior to the measurement of all force curves; a relative humidity meter (Digitron 2080R, Devon, England) was used to ensure the relative humidity remained below 3% throughout the experiment. On each of five granules, force curves were recorded at up to 16 different locations on the surface, with each of the locations separated by at least 1 μm. The shapes of the AFM probe tips were characterised using the reverse tip imaging technique; each probe was used to scan a grating comprised of an array of ultra sharp spikes (TGT-1, NT-MDT, Moscow, Russia), producing multiple tip images, which were then used to calculate the contact radius of the tip used [25]. All imaging data were analysed using Nanoscope™ software version 6.13. Each image was processed using the 'first order flatten' command within the software to remove the effect of tilt on the sample. All force curve data were analysed using Excel (Microsoft, 2003).

2.5. Nitrogen adsorption

Portions of the excipient powders (approx. 2.25–2.65 g) were dried at 106 °C under vacuum for 1 h. Nitrogen adsorption isotherms were measured in triplicate, at liquid N_2 temperature (−196 °C), using an automated Tristar 3000 apparatus (Micromeritics, Norcross, GA, USA). For each specimen, a total of 32 adsorption measurements were performed as the partial pressure was increased incrementally over the range 0.029–0.99, followed by a further 24 measurements under decreasing pressure. In each case, the equilibration time was 30 s. The results were analysed using the classical BET theory for surface adsorption [26], the version derived by Mahnke and Mögel [27] for adsorption onto fractal surfaces and the BJH model for capillary condensation [28].

2.6. Small-angle X-ray scattering

SAXS studies were performed using a Nanostar camera (Bruker AXS Inc. Madison, WI, USA), fitted with a sealed microbeam source, which was run at 40 kV, 35 mA and filtered to give Cu Kα radiation (wavelength, λ_X = 0.154 nm). The sample to detector distance was approximately 1.05 m and the entire optical path, including sample chamber, was evacuated. Two-dimensional scattering (2D-SAXS) patterns were collected using a Hi-Star gas-filled wire grid area detector, with a circular cross-section lead 'beamstop' suspended ahead of the detector, to absorb the undeviated X-ray beam. The scattering angle (2θ) was calibrated using a silver behenate powder sample and the modulus of the scattering vector was calculated using:

$$q = |q| = \frac{4\pi . \sin\theta}{\lambda_X} \quad (1)$$

Uncompacted powder specimens of MCC and PGS, approximately 1 mm thick, were mounted in a sample holder between thin mica sheets (Attwater Group, Preston, UK) and SAXS patterns were acquired in 'transmission' geometry. Acquisition times of 15 min were used and corrections for 'background scattering' were performed, after allowing for X-ray absorbance due to the specimens. SAXS intensity curves were extracted from the 2D-SAXS patterns using SAXS for Windows® NT software (Bruker AXS Inc. Madison, WI, USA); unidirectional 'q-scans' were obtained by azimuthal integration over the entire 2D-SAXS patterns, with increments in the scattering angle (2θ) of 0.01°.

2.7. Wide-angle X-ray scattering

WAXS powder patterns were collected using a Philips X'Pert system (PANalytical B.V. Almelo, Netherlands), using Cu Kα illumination. MCC and PGS specimens were supported in 15 mm aluminium frame and scanned over an angular range of 2θ = 4–50°, at 0.05° steps, 3 s at each step.

3. Results

3.1. Small- and wide-angle X-ray scattering

SAXS data for s-MCC and PGS granules are shown in Fig. 1. Both 2D-SAXS patterns were circularly symmetrical, as expected for randomly oriented granules or isotropic intragranular sub-structure. The scans of intensity *vs.* scattering vector were essentially

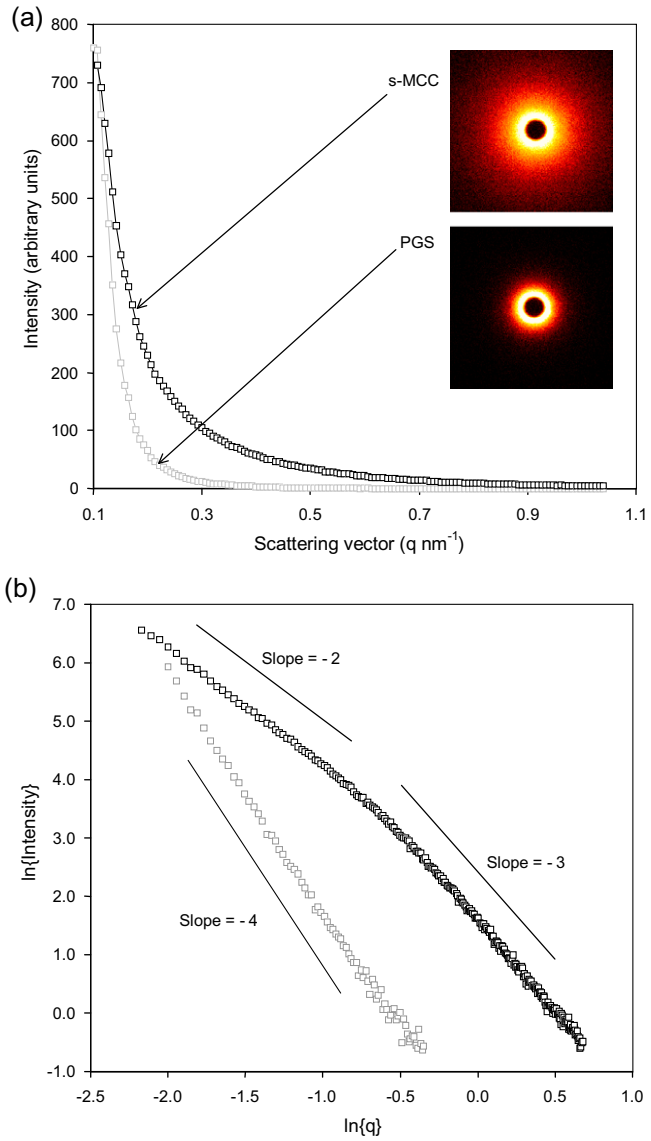

Fig. 1. SAXS data for s-MCC and PGS: (a) linear axes, inserts show 2D-SAXS patterns and (b) double-logarithmic plots, straight lines show slopes for comparison. (For interpretation of the references to colour in this figure legend, the reader is referred to the web version of this article)

featureless, in the form of smoothly decreasing curves from the edge of the beamstop shadow (at $q = 0.1$ nm^{-1}), indicating the lowest observable scattering angle, until the data merged with the background, at higher q. The only apparent difference between the two materials was that the scattering from PGS decreased to the level of the background more rapidly, over a shorter q-range ($q < 0.5$ nm^{-1}), compared with s-MCC ($q > 0.9$ nm^{-1}).

Plotting on double-logarithmic axes revealed the data in the form of fairly straight lines, roughly indicative of 'power-law' scattering behaviour:

$$I(q) = I_0 \cdot q^{-\alpha} \quad (2)$$

where the constant I_0 depends on the scattering contrast within the material, acquisition time, intensity of the X-ray illumination, etc. and α is the power-law constant. Power-law scattering is often interpreted in terms of 'fractal' structures [21,29] even though: (i) it can also be exhibited by materials with porous or other morphologies that do not show the strict self-similarity over different length-scales expected for a true fractal; (ii) for 'physically real' materials, fractal behaviour must break down at small lengths approaching the atomic scale and at large lengths approaching the specimen size. Notable examples of the former include $\alpha = 1$ dependence shown by systems composed of thin rods and the $\alpha = 2$ dependence shown by thin disks or 'Gaussian' polymer chains [21,22]. Moreover, according to Porod's law [21,30], any scattering system composed of two homogeneous phases with topologically smooth and compositionally sharp interfaces will show $\alpha = 4$ dependence towards higher q.

The PGS data appeared to follow Porod's law fairly well, with $\alpha \approx 4$, over the entire observable q-range, which suggested a structurally irregular but strictly two-phase system. Other materials reported to exhibit $\alpha = 4$ dependence include some types of porous glass and limestone [29]. Closer examination revealed a slight curvature, with a small but apparently systematic variation in the power-law constant, from $\alpha = 4.3$ at low q to $\alpha = 3.6$ at high q. The former condition ($\alpha > 4$) may indicate a deviation from compositionally sharp interfaces as measured over larger length-scales (>20 nm), while the latter may indicate interfacial roughness over small length-scales (<5 nm) [21,30,31]. Significantly, interfacial roughness over short length-scales could account for the apparent compositional blurring over longer length-scales; hence, the variations in power-law constant observed at low and high q may be due to the same structural features. The temptation to over-analyse this SAXS data should be avoided, however, since it was only measurable over a relatively short q-range, with the apparatus used here.

Many previous workers used SAXS to investigate the structure of starch granules, including Vermeylen et al. [32] and Suzuki et al. [33] who interpreted the scattering in terms of fractals. These studies demonstrated the progressive disappearance of the concentric semi-crystalline shell structure present in 'native' starch during gelatinisation; however, no account of any structure developed after gelatinisation could be found.

The SAXS data for s-MCC showed two straight sections, corresponding to $\alpha = 2$ for $\ln(q) < -0.7$ and $\alpha = 3$ for $\ln(q) > -0.3$. This suggested a change in the s-MCC structure at a characteristic length around $1/q = 1.6$ nm. It may be significant that this length is comparable to the width of elementary fibrils of native cellulose [34]. SAXS data from cellulose were previously interpreted in terms of fractals by Lin et al. [35], who reported power-law constants ranging from 2.13 to 2.73 or 3.93 to 4.07, for different fibrous materials; however, these authors did not examine granular MCC.

The value of the power-law constant at lower q ($\alpha = 2$) suggested an intragranular sub-structure showing characteristics of a mass fractal with dimensionality of two, over longer length-scales. Since this fractal-like structure is embedded in three-dimensional space, it suggested a loose connectivity and incomplete space-filling; however, this may involve two interpenetrating solid phases and porosity cannot be concluded from the SAXS data alone.

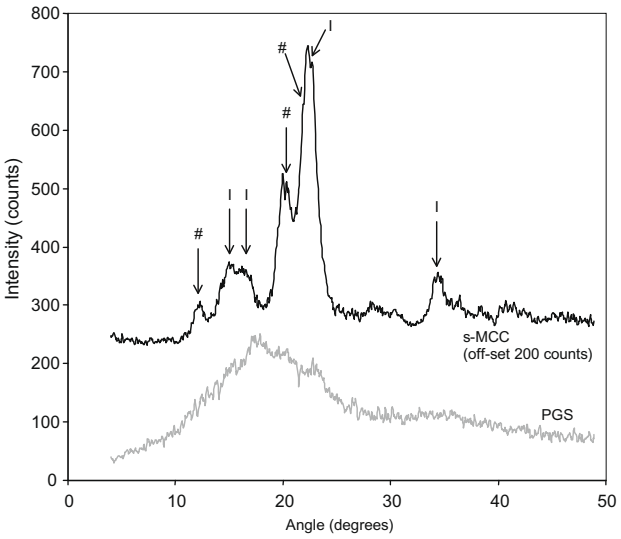

Fig. 2. WAXS data for s-MCC (off-set upwards by 200 counts for ease of viewing; I indicates cellulose I polymorph, # indicates cellulose II polymorph) and PGS.

At first sight, the scattering behaviour observed at higher q (with $\alpha = -3$) is less easily explained. Mass fractals are expected to show power-law behaviour with $\alpha < 3$, while surface fractals are expected to give $\alpha > 4$. This can be further modified, however, by the presence of density variations within the phases and by irregular or diffuse interfaces [21,30,31]. Hence, the data suggest a complex structure for s-MCC over small length-scales, which cannot be elucidated on the basis of SAXS alone.

WAXS data for PGS and s-MCC is shown in Fig. 2. There were no clear peaks observable for PGS, suggesting that this material was essentially non-crystalline: either the volume fraction of any crystalline material was small or the crystals must have been small (less than a few nanometres), producing broad peaks. By contrast, the s-MCC data showed several strong (albeit, still relatively broad) peaks, typical of semi-crystalline polymers, over relatively little 'amorphous background'. Comparison with published data [34,36–38] suggested that the Celphere s-MCC contained a mixture of the (native) cellulose I and (regenerated) cellulose II polymorphs. Significantly, the presence of cellulose I indicated the persistence of elementary fibrils from the original plant material, which was consistent with the change in power-law constant in the SAXS data. Conversely, the presence of cellulose II suggested that some of the s-MCC material had undergone dissolution or extensive swelling in alkali, possibly during the spheronisation process.

3.2. Electron microscopy and atomic force microscopy of s-MCC

Typical SEM, TEM and AFM images of s-MCC are shown in Fig. 3, which revealed a range of structural features. Examination at relatively low magnification (Fig. 3a and b) showed that the s-MCC granules were roughly spherical, with diameters generally between 50 and 200 μm and uneven surfaces suggestive of micrometre-scale internal structures. Embedding and fracturing revealed a heterogeneous internal structure, with what could be the remnants of plant cell walls and regions of apparent porosity on the scale of 0.2–2 μm (Fig. 3c).

Examination of a stained section by TEM revealed variations in electron transparency, indicating differences in stain uptake over length-scales from 500 nm to below 100 nm (Fig. 3d). It is likely

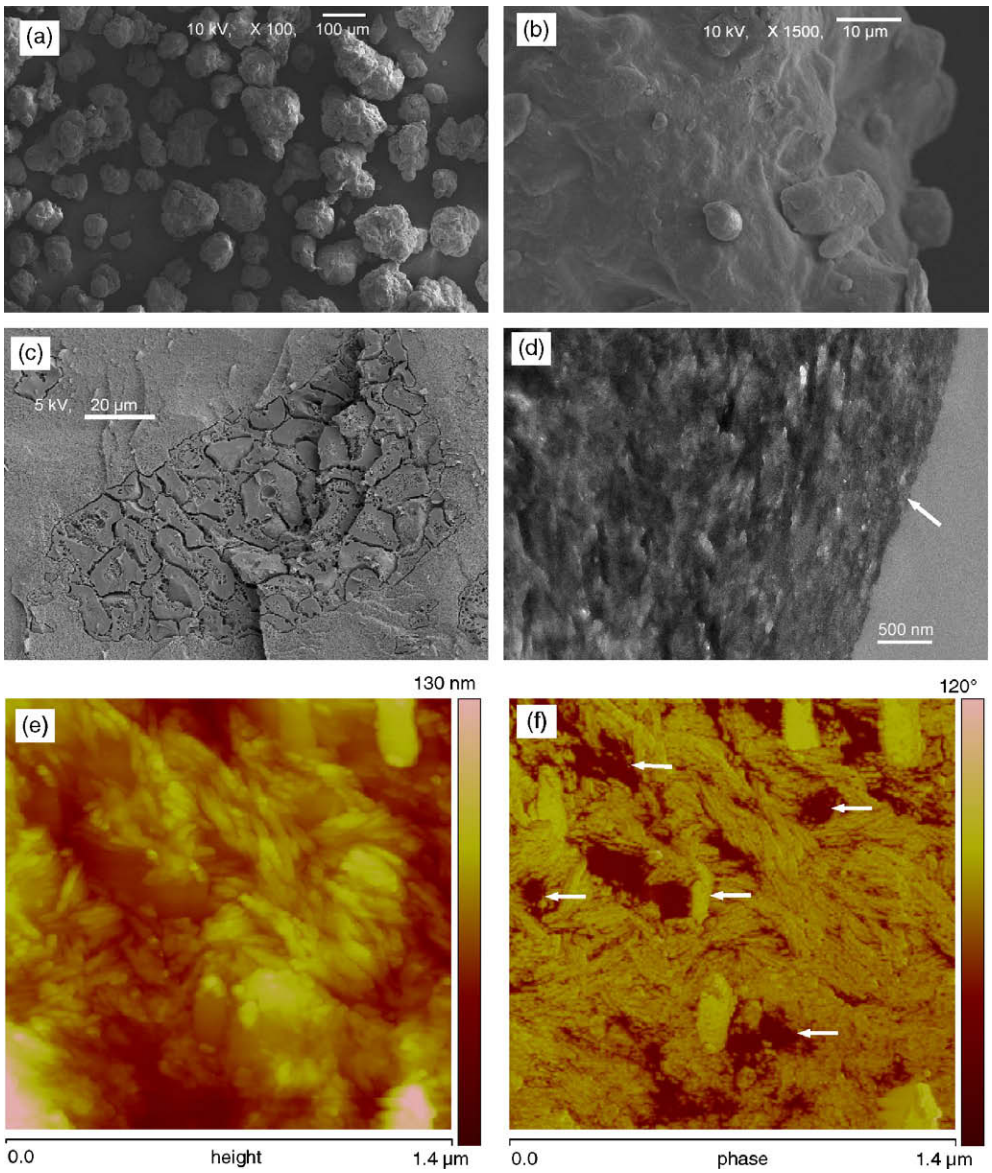

Fig. 3. Microscopy data for s-MCC: (a) and (b) SEM of granules on adhesive carbon tape; (c) SEM of granule embedded in resin, then fractured; (d) TEM; (e) AFM topology (height) and (f) AFM phase images (arrows indicate areas of contrast in the phase image not matched by contrast in the height image). (For interpretation of the references to colour in this figure legend, the reader is referred to the web version of this article)

that the darker (more heavily stained) regions incorporated porosity on the scale of a few nanometres (i.e. below the spatial resolution of the original TEM image), into which the heavy metal salts could penetrate more easily. Beyond about 1 µm from the granule surface (marked with an arrow in Fig. 3d), the distribution of regions with lighter or heavier staining appeared to become coarser. Similar changes were also observed in other TEM images; comparison with the SEM image (Fig. 3c) suggested that this may have been due to differences in porosity between the cell wall material and lumen of plant-fibre residues, located close to the granule surface. In addition, a few very light regions (i.e. even lighter than the embedding resin, observable to the right of Fig. 3d) were found, with dimensions less than 200 nm. These appeared to be holes, which may indicate 'open' porosity (i.e. lacking material to absorb the stain) or damage while preparing the section.

Representative AFM height and phase images (Fig. 3e and f, respectively) revealed an abundance of short rod-like features on the surface of an s-MCC granule. These features appeared to be consistent with fragments of elementary fibril bundles from the original plant material [34]. The apparent diameter of these features was comparable to the radius of curvature of the AFM probe tip (10–20 nm), however, so these images were expected to be subject to tip convolution effects [39].

Phase imaging is a derivative of tapping mode imaging [40]. By measuring the phase lag between the driving oscillation and the cantilever oscillation as the cantilever moves across the sample surface, a phase image can be constructed. Contrast in phase imaging facilitates the detection of variations in the physico-mechanical properties (e.g. composition, adhesion, friction, viscoelasticity) of a surface [41,42]. Areas of phase contrast that were independent of variations in surface topography have been highlighted with arrows (Fig. 3f); this gave a qualitative indication of heterogeneity on the s-MCC granule surface.

Representative force–displacement curves recorded on the surface of s-MCC granules are shown in Fig. 4. The data shown in Fig. 4a and b were recorded on the same granule surface at locations separated by more than 1 µm. The differences in shape illustrate the heterogeneity in surface material responses to the application of a loading force; this in line with inferences from comparisons between height and phase images (Fig. 3e and f). In

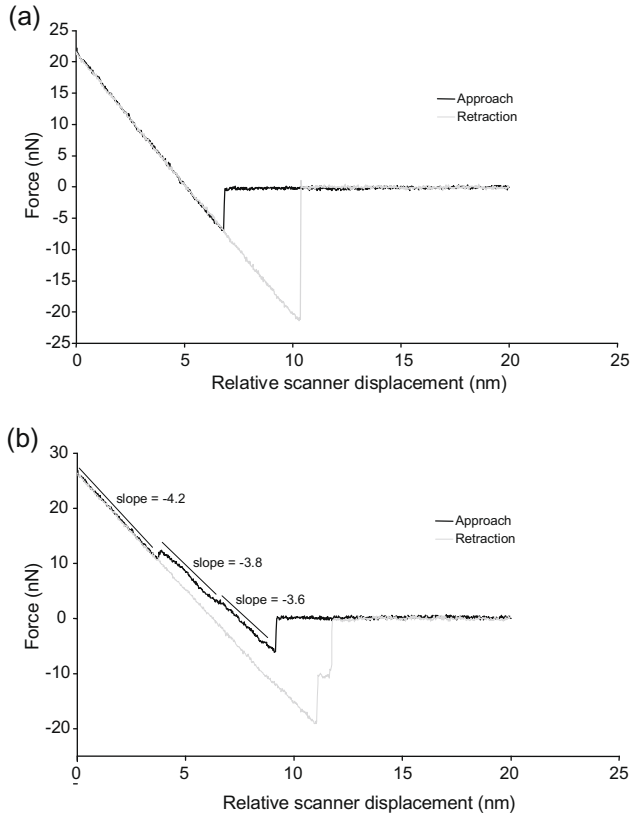

Fig. 4. Force–displacement curves recorded on the surface of s-MCC granules (a) shows (ideal) linear behaviour (b) shows nonlinear behaviour with steps in the approach curve.

Fig. 4a, the linear correlation between loading force and scanner displacement during both approach and retraction illustrated a linear response in surface indentation to the application of the loading force. Such a response represented an elastic indentation by the probe on the sample [43] and was observed in the majority of force–displacement curves. The results in Fig. 4a gave a loading force of approximately 25 nN, although considerable variations were observed between measurements at different locations. Using an adaptation [43] of Hertz contact theory [7], the Young's modulus (E) of the surface was then estimated according to:

$$E = \frac{3F(1-\nu^2)}{4\sqrt{r_{tip}\sigma^3}} \quad (3)$$

where F is the loading force applied by the AFM cantilever, ν is the Poisson's ratio (taken to be 0.3) and r_{tip} is the contact radius of the tip. The indentation depth (σ) was measured using:

$$\sigma = \Delta z - \Delta_{def} \quad (4)$$

where Δz is the relative piezo scanner displacement and Δ_{def} is the resulting cantilever deflection during the approach curve of the force loading cycle [25].

The distribution of modulus results is summarised by the histogram in Fig. 5. The majority of results fell between 1 and 5 GPa, which compared well with the value of 5.7 GPa reported by Hancock et al. from thermomechanical measurements made on small microcrystalline cellulose compacts [44]. However, measurements at several locations yielded significantly higher modulus values (up to 54 GPa). Using inelastic X-ray scattering, Diddens et al. [45] observed strong anisotropy in E for oriented bundles of flax fibres. Modulus values measured parallel to the fibre axis ($E_{||}$ = 220 GPa) were considerably larger than those measured perpendicular to

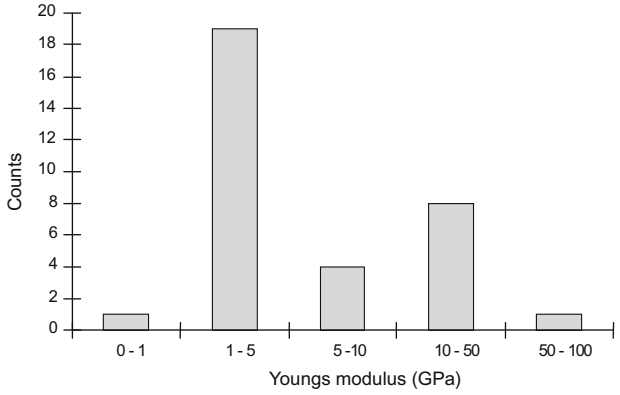

Fig. 5. Histogram illustrating the distribution of Young's modulus values calculated from force–displacement curves showing linear behaviour on s-MCC.

the fibres ($E_{\perp}$ = 15 GPa), which was attributed to the differences in bonding (i.e. covalent along the cellulose chains parallel to the fibre axis; van der Waals forces perpendicular to the fibres). The highest modulus values obtained in the present work for s-MCC granules were more than four times lower than $E_{||}$ reported by Diddens et al., while the majority were even less than $E_{\perp}$. It seems likely that this was due to the disordered packing and relatively weak interactions (i.e. van der Waals forces or material bridges) between microfibrils within the s-MCC granules. Moreover, inspection of the height image (Fig. 3e) revealed that the cellulose fibrils at the surface of the s-MCC granules lay at a variety of orientations, which may account for the range of modulus values obtained here.

Fig. 4b shows a representative force–displacement curve recorded at a site where the surface demonstrated nonlinear behaviour. Such nonlinear behaviour suggested a more complex interaction between the probe and the sample at that site on the surface. The changes in slope evident in the approach curve were believed to result from a non-elastic deformation of the s-MCC granule surface, caused by the AFM probe. As the Hertz model assumes elastic deformation, only the first section of the approach curve, before non-elastic deformation occurred, could be used to obtain a value for Young's modulus [43]. Calculation of Young's modulus in this way led to values below 1 GPa (average of 0.43 GPa, n = 27), which was far less than the values calculated for sites that showed a linear response.

The more complex interactions, which resulted in force–displacement curves similar to that shown in Fig. 4b, were thought to originate from differences in the material properties of the granule surface at that point, related to the underlying morphology of the s-MCC granule. The approach curve indicated a sudden partial collapse of the surface as the loading force was gradually increased. A step was also seen in the retraction curve as the probe moved away from the granule surface, which suggested that the surface relaxed as the force applied during the loading cycle was removed. This compression and relaxation behaviour appeared to be consistent with discrete regions of very soft and easily deformed material or nanoscale porosity, at some locations just below the s-MCC granule surface.

3.3. Electron microscopy and atomic force microscopy of PGS

Typical SEM and AFM images of PGS are shown in Fig. 6. At a superficial level (Fig. 6a), the PGS granules exhibited a wider diameter distribution and appeared more angular, compared with s-MCC. Closer examination of the surface at higher magnification (Fig. 6b) or after embedding and fracturing (Fig. 6c) revealed layers of spheres of roughly 200–400 nm diameter (Fig. 6d). Spherical

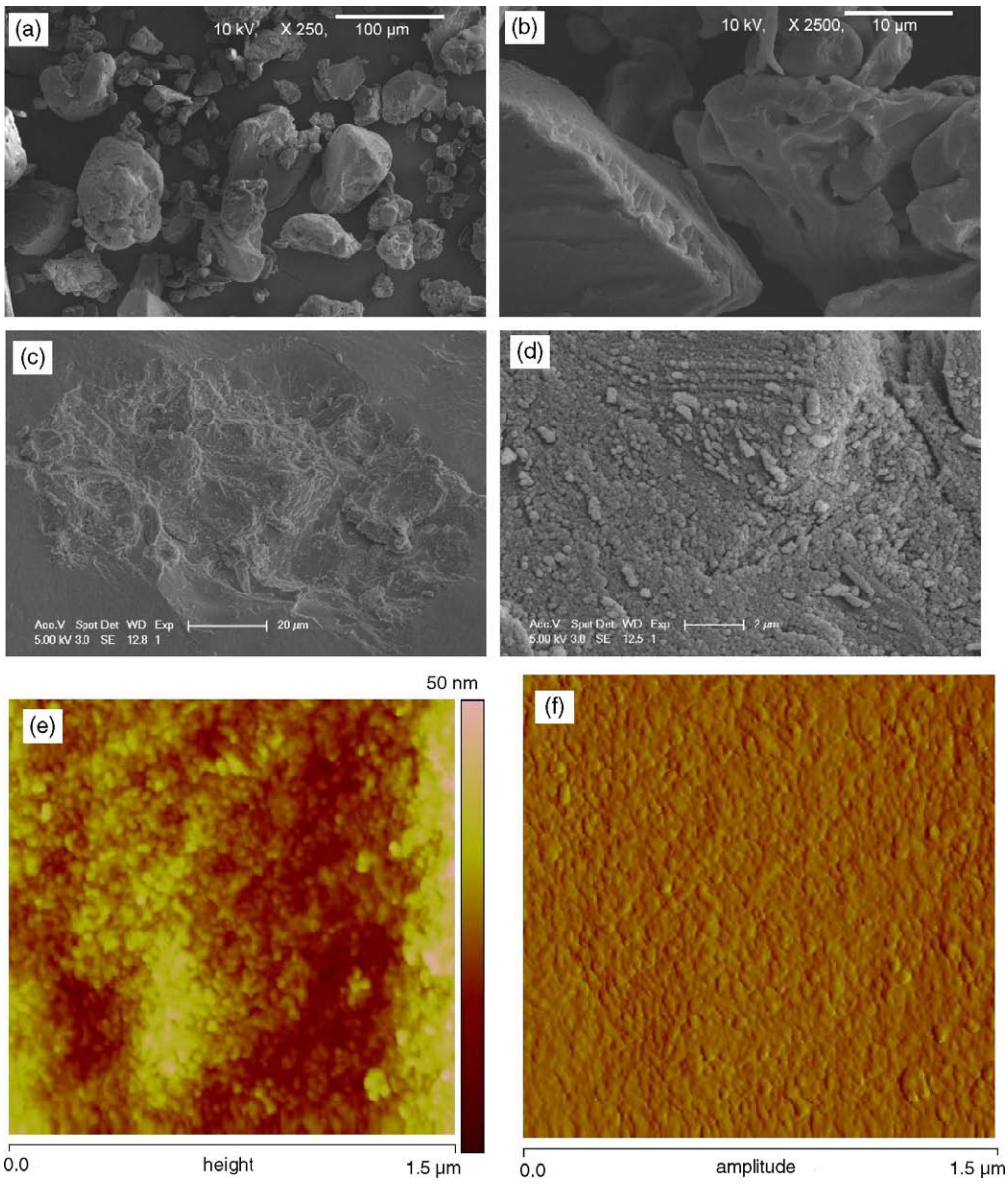

Fig. 6. Microscopy data for PGS: (a) and (b) SEM of granules on adhesive carbon tape; (c) and (d) SEM of granule embedded in resin, then fractured; (e) and (f) AFM height and amplitude images. (For interpretation of the references to colour in this figure legend, the reader is referred to the web version of this article)

sub-structures with diameters in the region of 25 nm were also revealed by AFM (Fig. 6e and f, height and amplitude, respectively), which may be associated with highly branched amylopectin molecules.

No topography-independent phase contrast was observed on the surfaces of PGS granules. Force–displacement curves recorded on granule surfaces did not demonstrate linear behaviour during the loading force cycle. Moreover, in order to indent the PGS surface, it was necessary to use cantilevers with higher spring constants (up to 40 N m^{-1}) than those used on s-MCC granules. The bending pattern followed by approach curves during the force loading regime was complex and showed evidence of viscoelastic behaviour (not shown here). No further analysis was undertaken on this data, at this stage.

3.4. Nitrogen adsorption

The measurement of gas adsorption isotherms is widely used to investigate porous materials [46] and, after a suitable treatment of the data, may be expected to provide a useful comparison with the microscopy results. Adsorption onto flat surfaces is commonly analysed using the multilayer BET model [26], which describes the relationship between the quantity adsorbed and the partial pressure (i.e. pressure divided by the saturation vapour pressure, $p = P/P_0$) of the gas:

$$V = \frac{V_m \cdot C \cdot p}{(1 - p + Cp)(1 - p)} \tag{5}$$

V_m is the adsorbed quantity for monolayer coverage and C is a constant that describes the relative preference for mono-molecular adsorption compared with multilayer formation:

$$C \approx \exp\left\{\frac{H_1 - H_L}{RT}\right\} \tag{6}$$

where H_1 and H_L are the heats of desorption from a monolayer and evaporation from a multilayer, respectively. It is often more convenient to rearrange Eq. (5) into a linearised form:

$$\frac{1}{V\left(\frac{1}{p}-1\right)} = \frac{1}{V_m \cdot C} + \frac{(C-1)}{V_m \cdot C} \cdot p \tag{7}$$

Hence, plotting the quantity on the left of Eq. (7) against the partial pressure should give a straight line, from which the values of C and V_m can be obtained. The surface area (S) can then be estimated from V_m and the area occupied per molecule (0.162 nm^2, for N_2 [46]).

The BET model assumes that the surface area available is independent of the number of adsorbed mono-molecular layers (i.e. the thickness of the adsorbed layer). Hence, the quantity adsorbed is proportional to the average thickness of the adsorbed layer, which is governed by the partial pressure and the energetics of mono-molecular or multilayer condensation [26]. This is valid for flat, two-dimensional surfaces, but breaks down for more complex topologies, including rough or porous surfaces. In these cases, the presence of an adsorbed layer can smooth over the uneven surface, causing a decrease in the effective surface area as the adsorbed layer thickness increases with partial pressure. This has led to the concept of adsorption onto fractal surfaces, requiring some modification of the classical BET model, as discussed by Pfeifer and co-workers [47,48] and Mahnke and Mögel [27], amongst others. According to the 'fractal model' derived by Mahnke and Mögel [27]:

$$V = \frac{V_m \cdot C \cdot p}{(1-p+Cp)(1-p)^{(3-D)}} \tag{8}$$

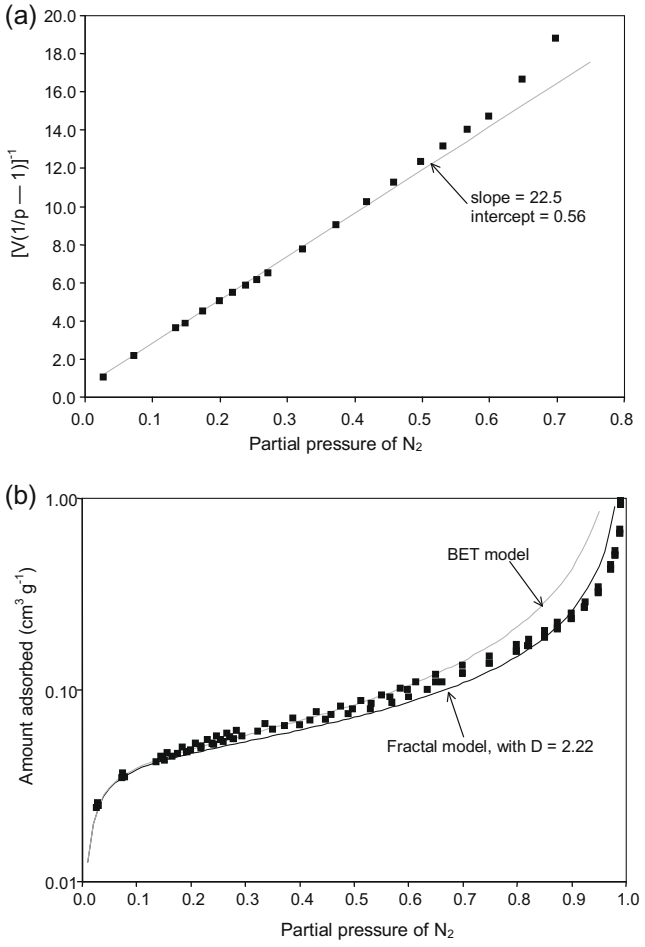

Fig. 7. Nitrogen adsorption isotherm results for s-MCC: (a) linearised plot at low partial pressure (fitted to data for $p < 0.4$), (b) amount adsorbed vs. partial pressure, in comparison with BET model (derived from linear fit in a) and fractal model after Mahnke and Mögel [27] (best fit over entire data range, but using C and V_m obtained from linearised fit, in a).

Table 1
Summary of adsorption results for s-MCC and PGS.

	Results for	
	s-MCC	PGS
C	41	72
V_m (cm^3 at STP g^{-1})	0.043	0.048
Mono-molecular coverage at p	0.135	0.105
S (m^2 g^{-1})	0.19	0.21
H_1 (kJ mol^{-1})	8.0	8.3
Fractal dimension	2.22	2.50

where D is the fractal dimension of the surface. It may be noted that Eq. (8) reverts to the BET equation, for flat, two-dimensional surfaces, where $D = 2$.

Nitrogen adsorption data for s-MCC is presented in Fig. 7, in comparison with the classical BET and fractal surface adsorption models. The linearised experimental data fitted the BET model well at low partial pressures, but significant positive deviations (upward curvature) occurred for $p > 0.4$, as shown in Fig. 7a. Fitting a linear regression line to the data for $p < 0.4$ yielded the values of C, V_m and S shown in Table 1. The BET model generated using these values fitted the experimental data well at low partial pressures, but showed progressively worsening positive deviations for $p > 0.6$ (corresponding to adsorbed quantities greater than about 0.11 cm^3 g^{-1}). It appeared that N_2 adsorption onto s-MCC fell short of expectations based on the BET model, for multimolecular layers with $V/V_m > 2.5$. This was consistent with the presence of surface roughness or porosity approaching the molecular scale (characteristic lengths <1 nm).

Better agreement with the experimental data at high partial pressures was obtained using the 'fractal model' of Manke and Mögel [27]. The curve in Fig. 7b was also generated using the values of C and V_m obtained from the linearised plot and manually fitted over the entire data range by selecting the value of D. This suggested a fractal dimension of $D = 2.22$, although there were still small deviations between the model and experimental data over much of the pressure range (approximately $0.2 < p < 0.8$ and $p > 0.9$). A closer fit could be obtained using different values of C and V_m, but these appeared to be incompatible with the linearised data at low p.

A similar analysis of the data for N_2 adsorption on PGS is shown in Fig. 8. In this case, fitting the regression line was restricted to $p < 0.3$, since significant upward curvature was observed for the experimental data at higher partial pressures, as shown in Fig. 8a. The results of this analysis are given in Table 1. The corresponding BET and fractal models, generated using these values of C and V_m, are compared with the experimental data in Fig. 8b. It was found that the BET model predicted adsorption significantly in excess of the experimental values for $p > 0.3$ (corresponding to adsorbed quantities greater than about 0.07 cm^3 g^{-1} or $V/V_m > 1.5$), suggesting surface roughness or porosity on the molecular scale for PGS. Again, a closer, though not perfect fit was obtained using the 'fractal model', with $D = 2.5$.

The values obtained for C were larger than those reported by Strømme et al. for adsorption onto various types of cellulose [49], but within the usual range expected for N_2 adsorption [46]. Assuming that H_L in Eq. (3) was the same as for vaporisation from bulk liquid (5.57 kJ mol^{-1} [50]), this gave values of H_1 in the range 8.0–8.3 kJ mol^{-1}.

The values of V_m were comparable with those reported previously by Strømme et al. [49] for MCC, indicating relatively small surface areas (0.19–0.21 m^2 g^{-1}) for the materials studied here. By way of comparison, Khalili et al. reported surface areas between 28 and 1207 m^2 g^{-1} for a selection of absorbent carbon materials [51], Du and Wu reported between 32 and 565 m^2 g^{-1} for various

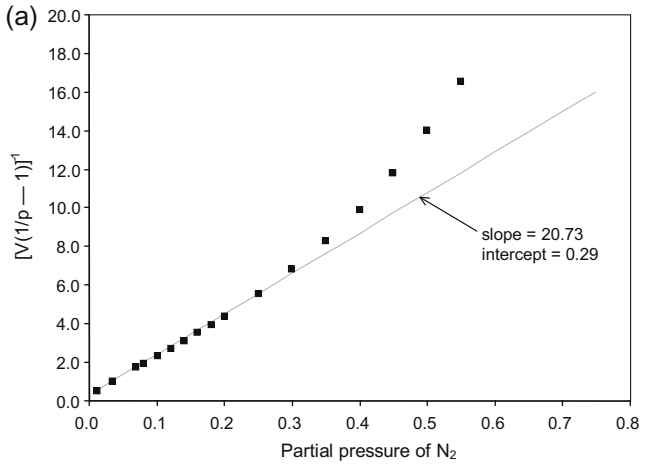

Fig. 8. Nitrogen adsorption isotherm results for PGS: (a) linearised plot at low partial pressure (fitted to data for $p < 0.3$), (b) amount adsorbed vs. partial pressure, in comparison with BET model (derived from linear fit in a) and fractal model after Mahnke and Mögel [27] (best fit over entire data range, but using C and V_m obtained from linearised fit, in a).

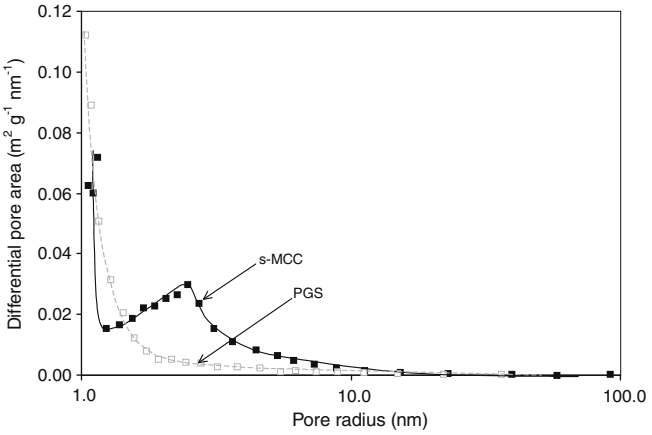

Fig. 9. Differential pore area vs. size distributions for s-MCC and PGS.

zeolites [52] and Reddy et al. reported 2.2 $m^2\,g^{-1}$ for a 'welded tuff' rock sample [53]. The relatively small values of surface area for s-MCC and PGS suggested that most of the interfaces between the sub-structural features indicated by microscopy were occluded in some way and unavailable to N_2 adsorption – although this may have been due to no more than a surface layer of impermeable material around the granules. Significantly, Strømme et al. [49] reported considerably greater surface areas for measurements using water vapour (which can swell amorphous cellulose), compared with nitrogen (which is not expected to cause any swelling).

As a further guide, for a material with a 'true' density of 1600 $kg\,m^{-3}$ (similar to s-MCC and PGS) in the form of a solid sphere and a surface area of 0.2 $m^2\,g^{-1}$, its radius is given by:

$$r = \frac{3}{S\rho} = 9.4\ \mu m \tag{9}$$

This is between two and three orders of magnitude larger than the length-scales expected for features observable by SAXS, although still considerably smaller than typical granule diameters. Clearly, adsorption measurements were only able to probe the accessible aspects of the s-MCC or PGS granules, which probably did not include the main features responsible for the X-ray scattering. It should be noted that SAXS did not require pores accessible to N_2 adsorption – only variations in electron density, which were clearly evident from microscopy. Hence, this explains why the fractal dimensions indicated by adsorption experiments did not match the power-law constants from SAXS data.

A further complication in interpreting gas adsorption data may be due to capillary condensation in micropores. This may be analysed using the BJH model [28], where differential pore volume is estimated from the quantities of N_2 adsorbed and the corresponding pore diameter is related to the mean radius of curvature (r_m), which is estimated using the Kelvin equation:

$$\ln(p) = \frac{2\gamma V_{mol} \cdot \cos\theta}{RTr_m} \tag{10}$$

where γ and V_{mol} are the surface energy and molar volume of the condensate ($8.85 \times 10^{-3}\,J\,m^{-2}$ and $34.65 \times 10^{-6}\,m^3\,mol^{-1}$ for N_2), θ is the contact angle (assumed $\theta = 0$, for N_2 adsorption), R is the gas constant ($8.314\,J\,K^{-1}\,mol^{-1}$) and T is the temperature (77 K). The version programmed into the Tristar software also allowed for the thickness of the adsorbed layer on the pore walls at the corresponding partial pressure, based on the BET model.

Pore-size distribution results for s-MCC and PGS are shown in Fig. 9. Both materials appeared to contain small amounts of porosity, predominantly with $r_m < 10$ nm and increasing towards the molecular scale. There appeared to be negligible surface area associated with larger pores for either material. The absence of any significant hysteresis between measurements during pore filling and emptying (i.e. during the increasing and decreasing pressure stages of the experimental procedure) argued against the presence of 'bottle-shaped' pores, with small openings leading to larger interiors. In addition, differential pore area results for s-MCC, exhibited a small peak in the curve around $r_m = 2.5$ nm, which would appear to be consistent with pores between the fibril bundles.

4. Discussion

The main purpose of the present work was to elucidate the morphological features within s-MCC and PGS granules that give rise to the 2D-SAXS patterns from these materials, in order to better understand the changes observed following compaction [17,18]. In particular, detailed knowledge of the intragranular sub-structures would be very useful, in order to test the plausibility of the granule compaction hypothesis [23].

X-ray scattering in the small-angle range is associated with electron density variations over length-scales of roughly 1–100 nm [21]. Microscopy clearly revealed features matching these requirements, within both the s-MCC and PGS granules, which appeared to explain the SAXS patterns of these materials. In particu-

lar, the presence of hierarchical structures with characteristic dimensions ranging from nanometres up to micrometres and the lack of any obvious regular periodicity were entirely consistent with the rather featureless 'fractal-like' power-law scattering behaviour observed.

It was suggested previously [23] that the changes in 2D-SAXS patterns would be consistent with the intragranular sub-structure undergoing affine deformation during compaction. This is rather different from the Hertzian model [7] of local deformation and flattening of the contact point, which is usually assumed to operate between compacted granules [5,6]. Instead, the compacted granule was required to behave essentially similar to the macroscopic powder bed, but on a smaller scale. This is most likely to happen if the intragranular sub-structure actually comprises an assembly of flexible or loosely connected bodies, such that compaction may produce deformation and displacement throughout each granule. Clearly, the results from SEM, TEM and AFM examinations reported here appear to support that structural model for both s-MCC and PGS. Moreover, the ability to deform these structures was clearly indicated by the irregular force–displacement curves recorded on the surface of s-MCC granules and the viscoelastic behaviour of PGS granules, which adds credence to the postulated deformation mechanism. This mechanism also agrees with the compaction behaviour previously suggested by Johansson and co-workers [12–15] and Westermarck et al. [16].

The presence of intragranular porosity could not be deduced unambiguously from the microscopy data alone – although it was strongly inferred from the variations in staining observed by TEM and the force–displacement measurements made by AFM. Conversely, porosity was indicated by the BJH interpretation of the N_2-adsorption data, although the associated surface areas appeared to be surprisingly small, in view of the intragranular structures revealed by microscopy. These two apparently conflicting observations may be explained by the presence of relatively impenetrable surface material around the granules. Moreover, such a 'skin' could help to keep the granule intact, while allowing the internal sub-structures to move relatively freely during compaction.

The work presented here demonstrated links between the intragranular sub-structures and the observable SAXS patterns from the two materials studied. It also provided support for the granule deformation model that was previously proposed [23] to provide a quantitative explanation for the changes in 2D-SAXS patterns observed following compaction. Hence, this work provides a considerably stronger theoretical basis for using 2D-SAXS to investigate the sub-granular mechanisms of powder compaction behaviour.

5. Conclusions

Taking a consensus view from the very different methods used to study s-MCC and PGS, both materials exhibited hierarchical intragranular sub-structures, with characteristic dimensions ranging from nanometres up to micrometres, which were consistent with the power-law scattering observed. Moreover, these intragranular sub-structures appeared to be consistent with the granule deformation mechanism proposed previously [23] to explain the changes in the 2D-SAXS patterns observed following compaction. Hence, the work reported here provides a considerably stronger basis for using 2D-SAXS to investigate the sub-granular mechanisms of powder compaction behaviour.

Acknowledgement

The authors are extremely grateful to Pfizer plc. for generous funding.

References

[1] G. Alderborn, C. Nyström, Pharmaceutical Powder Compaction Technology, Marcel Dekker, Inc., New York, 1996.
[2] S. Patel, A.M. Kaushal, A.K. Bansal, Compression physics in the formulation development of tablets, Crit. Rev. Ther. Drug. Carr. Syst. 23 (2006) 1–65.
[3] I.C. Sinka, F. Motazedian, A.C.F. Cocks, K.G. Pitt, The effect of processing parameters on pharmaceutical tablet properties, Powder Technol. 189 (2009) 276–284.
[4] L.H. Han, J.A. Elliott, A.C. Bentham, A. Mills, G.E. Amidon, B.C. Hancock, A modified Drucker–Prager Cap model for die compaction simulation of pharmaceutical powders, Int. J. Solids Struct. 45 (2008) 3088–3106.
[5] N.A. Fleck, On the cold compaction of powders, J. Mech. Phys. Solids 43 (1995) 1409–1431.
[6] O. Skrinjar, P-L. Larsson, B. Storåkers, Local contact compliance relations at compaction of composite powders, J. Appl. Mech. 74 (2007) 164–168.
[7] H. Hertz, Über die Berührung fester elastischer Körper (Concerning the contact of solid elastic bodies), J. Reine Angew. Math. 92 (1882) 155–173.
[8] N. Rahmanian, M. Ghadiri, X. Jia, F. Stepanek, Characterisation of granule structure and strength made in a high shear granulator, Powder Technol. 192 (2009) 184–194.
[9] S. Boden, M. Bieberle, G. Weickert, U. Hampel, Three-dimensional analysis of macroporosity distributions in polyolefin particles using X-ray microtomography, Powder Technol. 188 (2008) 81–88.
[10] L. Farber, G. Tardos, J.N. Michaels, Use of X-ray tomography to study the porosity and morphology of granules, Powder Technol. 132 (2003) 57–63.
[11] D. Suteu, D. Bilba, F. Dan, Synthesis and characterization of polyamide powders for sorption of reactive dyes from aqueous solutions, J. Appl. Polym. Sci. 105 (2007) 1833–1843.
[12] B. Johansson, G. Alderborn, The effect of shape and porosity on the compression behaviour and tablet forming ability of granular materials formed from microcrystalline cellulose, Eur. J. Pharm. Biopharm. 52 (2001) 347–357.
[13] F. Nicklasson, B. Johansson, G. Alderborn, Tabletting behaviour of pellets of a series of porosities – a comparison between pellets of two different compositions, Eur. J. Pharm. Sci. 8 (1999) 11–17.
[14] B. Johansson, G. Alderborn, Degree of pellet deformation during compaction and its relationship to the tensile strength of tablets formed of microcrystalline cellulose pellets, Int. J. Pharm. 132 (1996) 207–220.
[15] B. Johansson, M. Wikberg, R. Ek, G. Alderborn, Compression behaviour and compactability of microcrystalline cellulose pellets in relationship to their pore structure and mechanical properties, Int. J. Pharm. 117 (1995) 57–73.
[16] S. Westermarck, A.M. Juppo, L. Kervinen, J. Yliruusi, Microcrystalline cellulose and its microstructure in pharmaceutical processing, Eur. J. Pharm. Biopharm. 48 (1999) 199–206.
[17] P.R. Laity, R.E. Cameron, A small-angle X-ray scattering study of local variations within powder compacts, Powder Technol. 192 (2009) 287–297.
[18] P.R. Laity, R.E. Cameron, A small-angle X-ray scattering study of powder compaction, Powder Technol. 188 (2008) 119–127.
[19] M. Sperl, Experiments on corn pressure in silo cells — translation and comment of Janssen's paper from 1895, Granul. Matter 8 (2006) 59–65.
[20] E.B. Pitman, Forces on bins: the effect of random friction, Phys. Rev. E 57 (1998) 3170–3175.
[21] R.-J. Roe, Methods of X-ray and Neutron Scattering in Polymer Science, Oxford University Press, New York, 2000.
[22] J.S. Higgins, R.S. Stein, Recent developments in polymer applications of small-angle neutron, X-ray and light scattering, J. Appl. Cryst. 11 (1978) 346–375.
[23] P.R. Laity, R.E. Cameron, Changes in small-angle X-ray scattering during powder compaction – an explanation based on granule deformation, Powder Technology, submitted for publication.
[24] J.E. Sader, J.W.M. Chon, P. Mulvaney, Calibration of rectangular atomic force microscope cantilevers, Rev. Sci. Instrum. 70 (1999) 3967–3969.
[25] J. Zhang, S. Ebbens, X. Chen, Z. Jin, S. Luk, C. Madden, N. Patel, C.J. Roberts, Determination of the surface free energy of crystalline and amorphous lactose by atomic force microscopy adhesion measurement, Pharm. Res. 23 (2006) 401–407.
[26] S. Brunauer, P.H. Emmett, E. Teller, Adsorption of gases in multimolecular layers, J. Am. Chem. Soc. 60 (1938) 309–319.
[27] M. Mahnke, H.J. Mögel, Fractal analysis of physical adsorption on material surfaces, Col. Surf. A. Physicochem. Eng. Aspects 216 (2003) 215–228.
[28] E.P. Barrett, L.G. Joyner, P.P. Halenda, The determination of pore volume and area distributions in porous substances. I. Computations from nitrogen isotherms, J. Am. Chem. Soc. 73 (1951) 373–380.
[29] P. Schmidt, Small-angle scattering studies of disordered, porous and fractal systems, J. Appl. Cryst. 24 (1991) 414–435.
[30] S. Ciccariello, On the Porod Law, J. Appl. Cryst. 21 (1988) 117–128.
[31] S. Tan, D. Zhang, E. Zhou, SAXS measurements of the interface in polyacrylate and epoxy interpenetrating networks with fractal interfaces, Polymer 38 (1997) 4571–4575.
[32] R. Vermeylen, V. Derycke, J.A. Delcour, B. Goderis, H. Reynaers, M.H.J. Koch, Gelatinization of starch in excess water: beyond the melting of lamellar crystallites. A combined wide- and small-angle X-ray scattering study, Biomacromolecules 7 (2006) 2624–2630.
[33] T. Suzuki, A. Chiha, T. Yano, Interpretation of small angle X-ray scattering from starch on the basis of fractals, Carbohydr. Polym. 34 (1997) 357–363.

[34] H.A. Krässig, Cellulose: Structure, Accessibility and Reactivity, Gordon and Breach Science Publishers, Yverdon, Switzerland, 1993.
[35] J.S. Lin, M-Y. Tang, J.F. Fellers, Fractal analysis of cotton cellulose as characterized by small-angle X-ray scattering, in: R.H. Atalla (Ed.), The Structures of Cellulose: Characterisation of the Solid State, ACS Symposium Series 340, 1987 (Chapter14).
[36] H.J. Wellard, Variation in the lattice spacing of cellulose, J. Polym. Sci. 13 (1954) 471–476.
[37] A.M. Hindeleh, D.J. Johnson, Crystallinity and crystallite size measurement in cellulose fibres: 1. Ramie and Fortisan, Polymer 13 (1972) 423–430.
[38] F.J. Kolpak, J. Blackwell, Determination of the structure of cellulose II, Macromolecules 9 (1976) 273–278.
[39] M.J. Allen, N.V. Hud, M. Balooch, R.J. Tench, W.J. Siekhaus, R. Balhorn, Tip-radius-induced artefacts in AFM images of protamine-complexed DNA fibres, Ultramicroscopy 42–44 (Part 2) (1992) 1095–1100.
[40] I. Schmitz, M. Schreiner, G. Friedbacher, M. Grasserbauer, Phase imaging as an extension to tapping mode AFM for the identification of material properties on humidity-sensitive surfaces, Appl. Surf. Sci. 115 (1997) 190–198.
[41] K.L. Babcock, C.B. Prater, Phase Imaging: Beyond Topography, Veeco Instruments Inc., Santa Barbara, CA, USA, 2004.
[42] A. Danesh, X. Chen, M.C. Davies, C.J. Roberts, G.H.W. Sanders, S.J.B. Tendler, P.M. Williams, M.J. Wilkins, Polymorphic discrimination using atomic force microscopy: distinguishing between two polymorphs of the drug cimetidine, Langmuir 16 (2000) 866–870.
[43] M. Perkins, S.J. Ebbens, S. Hayes, C.J. Roberts, C.E. Madden, S.Y. Luk, N. Patel, Elastic modulus measurements from individual lactose particles using atomic force microscopy, Int. J. Pharm. 332 (2007) 168–175.
[44] B.C. Hancock, S-D. Clas, K. Christensen, Micro-scale measurement of the mechanical properties of compressed pharmaceutical powders. 1: the elasticity and fracture behavior of microcrystalline cellulose, Int. J. Pharm. 209 (2000) 27–35.
[45] I. Diddens, B. Murphy, M. Krisch, M. Müller, Anisotropic elastic properties of cellulose measured using inelastic X-ray scattering, Macromolecules 41 (2008) 9755–9759.
[46] P.A. Webb, C. Orr, Analytical Methods in Fine Particle Technology, Micromeritics Instrument Corporation, Norcross, GA, USA, 1997.
[47] P. Pfeifer, D. Avnir, Chemistry in non-integer dimensions between two and three. 1. Fractal theory of heterogeneous surfaces, J. Chem. Phys. 79 (1983) 3558–3565.
[48] P. Pfeifer, M. Obert, M.W. Cole, Fractal BET and FHH theories of adsorption: a comparative study, Proc. Roy. Soc. Lond. A 423 (1989) 169–188.
[49] M. Strømme, A. Mihranyan, R. Ek, G.A. Niklasson, Fractal dimension of cellulose powders analyzed by multilayer BET adsorption of water and nitrogen, J. Phys. Chem. 107 (2003) 14378–14382.
[50] D.R. Lide, Handbook of Chemistry and Physics, CRC Press, Boca Raton, USA, 2002.
[51] N.R. Khalili, M. Pan, G. Sandí, Determination of fractal dimensions of solid carbons from gas and liquid phase adsorption isotherms, Carbon 38 (2000) 573–588.
[52] X. Du, E. Wu, Porosity of microporous zeolites A, X and ZSM-5 studied by small angle X-ray scattering and nitrogen adsorption, J. Phys. Chem. Solids 68 (2007) 1692–1699.
[53] M.M. Reddy, H.C. Claassen, D.W. Rutherford, C.T. Chiou, Welded tuff porosity characterization using mercury intrusion, nitrogen and ethylene glycol monoethyl ether sorption and epifluorescence microscopy, Appl. Geochem. 9 (1994) 491–499.